

A CME-driven shock analysis of the 14-Dec-2006 SEP event

Xin Wang^{1,2} and Yihua Yan¹

¹ National Astronomical Observatories, Chinese Academy of Sciences, Beijing 100012, China;
wangxin@nao.cas.cn

² State Key Laboratory of Space Weather, Chinese Academy of Sciences, Beijing 100080, China
Received 2012 April 12; accepted 2012 May 7

Abstract Observations of the interplanetary shock provide us with strong evidence of particle acceleration to multi-MeV energies, even up to GeV energy, in a solar flare or coronal mass ejection (CME). Diffusive shock acceleration is an efficient mechanism for particle acceleration. For investigating the shock structure, the energy injection and energy spectrum of a CME-driven shock, we perform dynamical Monte Carlo simulation of the 14-Dec-2006 CME-driven shock using an anisotropic scattering law. The simulated results of the shock fine structure, particle injection, and energy spectrum are presented. We find that our simulation results give a good fit to the observations from multiple spacecraft.

Key words: Acceleration of Particles, CME-driven Shock, Solar Energetic Particles, Numerical Simulation

1 INTRODUCTION

It is widely accepted that there are two classes of solar energetic particle (SEP) events, although recent observations indicate that the actual processes may be much more complicated (Pick & Vilmer, 2008). The first class is normal impulsive SEP events, which are connected with the large solar flare (Miller, 1997). The second class is gradual SEP events, which are responsible by diffusive shock acceleration (DSA) associating with fast coronal mass ejections (CMEs)(Cane, Reames, & von Roseninge, 1991; Yan et al., 2006). In solar magnetic connection region, CME and flares are two type of manifestations of the same magnetic energy release process (Wang et al., 1996; Zhang et al., 2001, 2007). Both CMEs and flares result in particle acceleration that constitute an SEP event. But which manifestation dominates the particle injection is still not clear (Li et al., 2009; Le et al., 2011; Qin & Shalchi, 2009). Some numerical models suggest that mixed particle acceleration by both flares and CME-driven shocks provide much better fits to the in-situ observations. Since the particle injection process is connected with the complicated nonlinear effects in the particle acceleration processes and also there exists difference of injection mechanism in two type of manifestations, so we just put forward to a pure shock numerical model to calculate the particle injection in the CME-driven shock. We expect that it would be helpful for understanding the particle injection problem in the SEP events.

DSA theory was first introduced in the later of 1970's (Krymsky (1977); Axford et al. (1977); Bell (1978); Blandford & Ostriker (1978). In the past several decades, the accumulation of the increasingly observational data from many spacecraft investigated the nonlinear diffusive shock acceleration (NLDSA) mechanism, which is the most efficient accelerator in many astrophysical and space physical environments (Bednarz & Ostrowski, 1999; Malkov & Drury, 2001; Bykov et al., 2009; Bykov & Treumann, 2011; Lu, Xia, & Wang, 2006; Zhang, Bi, & Hu, 2006). With the development of

technology in observational equipments, especially in spacecraft working in deep space, there are a lot of models for modeling the various nonlinear interaction with the diffusive shock acceleration. Several main approaches for studying the nonlinear DSA includes: the two-fluid model (Drury & Völk, 1981; Drury, Axford, & Summers, 1982); the numerical model (Berezhko & Völk, 2000; Kang & Jones, 2007; Zirakashvili, 2007; Verkhoglyadova et al., 2010); the stationary or dynamical Monte Carlo model (Ellison & Eichler, 1984; Knerr, Jokipii & Ellison, 1996; Vladimirov, Ellison & Bykov, 2006); the semi-analytical model (Malkov et al., 2000; Caprioli, Amato & Blasi, 2010) and etc. Among these approaches, the Monte Carlo method addresses the nonlinear effects of DSA by assuming that the entire particle population undergoes a random walk under a certain scattering law (Ellison, Möbius & Paschmann, 1990; Knerr, Jokipii & Ellison, 1996; Wang & Yan, 2011).

There are three important non-linear processes of DSA theory including the particle injection, particle confinement, and shock robustness (Malkov & Drury, 2001; Hu, 2009). Owing to the fact that walking processes of the particles can be controlled self-consistently in the Monte Carlo method, the Monte Carlo method has an advantage for simulating the particle injection. We have already studied the energy translation processes of an Earth-bow shock using the dynamical Monte Carlo method with a prescribed multiple anisotropic scattering angular distributions (Wang & Yan, 2012). We find that the acceleration efficiency increases as the dispersion of the scattering angular distribution increases from an anisotropic case to an isotropic case. Here, we will further investigate this important particle injection problem in the CME-driven shock using the dynamical Monte Carlo method. There exist a few different properties between the Earth-bow shock and the CME-driven shock: Firstly, Earth-bow shock has a stationary downstream bulk flow but the CME-driven shock has a dynamical downstream bulk flow; Secondly, the CME-driven shock front has an opposite motion compared with the Earth-bow shock's evolution; Thirdly, the CME-driven shock has an extended plane shock front structure near the Earth, but the Earth-bow shock front has a stationary bow shock geometry. We predict those differences would produce a different non-linear properties including the evolution of the shock fine structure, energy injection rate and even the energy spectral shape. This paper will focus on the understanding some of the non-linear properties of the planetary CME-driven shock. The 14-Dec-2006 shock event was fortuitous as it provides us an opportunity for applying the dynamical Monte Carlo package code, which was developed on the Matlab platform (Wang & Yan, 2011).

This paper is structured as follows: In Section 2, we present the specific observations for the 14-Dec-2006 CME-driven shock event; The detailed description of the method is given in Section 3; We present the simulated results and discussions in Section 4; Finally, Section 5 presents the summary and some conclusions.

2 OBSERVATIONS

The unusual group of CME-driven shock events of solar cycle 23 was observed in December 2006 at the solar active region 10930. Halo CMEs were observed by the LASCO coronagraphs in association with the events of 13 and 14 December, with speeds of 1774km/s and 1042km/s, respectively. Because the 14 December solar event was better magnetically connected to the Earth, so it provided the best opportunity for testing the nonlinear effect and efficiency of the diffusive shock acceleration (DSA) mechanism. As shown in Figure 1, an overview of key parameter observations from the Proton Monitor (PM) instruments on Wind/SWE for the CME shock event of 14 December 2006 is given in detail. This event originated on the western hemisphere of the Sun. It showed an abrupt fluctuation in intensity of proton density and solar wind thermal speed during the decay of the 13 December solar event. The initial particle increase following the 14 December solar event was seen in the higher energy range, as expected for velocity dispersion. There was also a higher background at the lower energy associated with the 13 December solar event and the related shock (von Rosenvinge et al., 2009). Simultaneously, many spikes were also detected to be superposed on the radio continuum in the frequency range 2.6-3.8 GHz by the digital spectrometers of NAOC. These spikes were found to have complex structures associated with other radio burst signatures connecting with the in-situ SEP event observations (Wang et al., 2008).

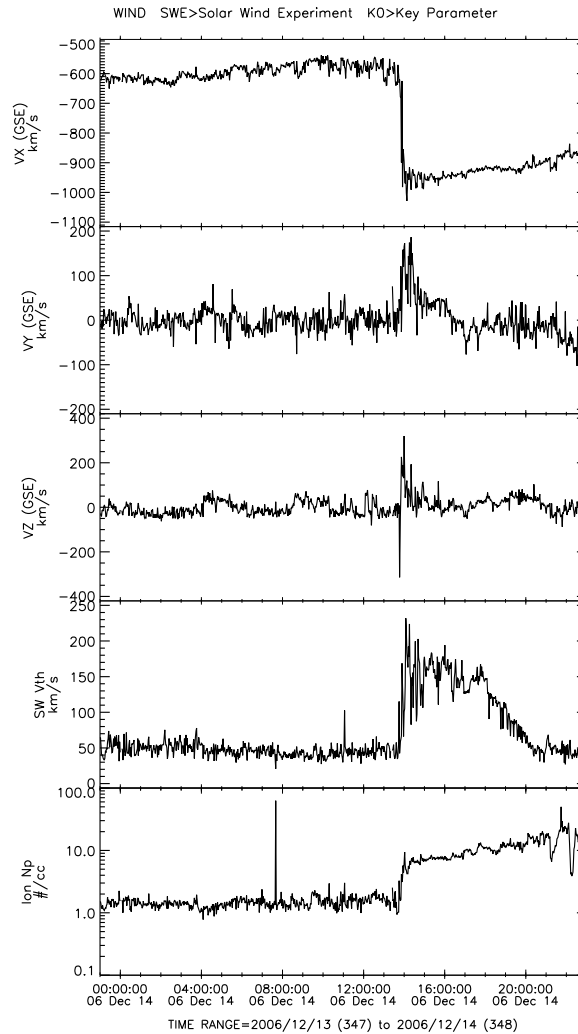


Fig. 1 The plot shows the key parameters of the 14-Dec-06 shock event in the Wind spacecraft, and the data come from <http://cdaweb.gsfc.nasa.gov/cdaweb>.

Both Wind and ACE were in orbit around the $L1$ Lagrangian point ~ 1.5 million km upstream of the Earth. Similar intensity modulations were observed at Wind and ACE. As has also been noted by Mulligan et al. (2008), the variations of the particle intensity and smooth magnetic fields observed by near-Earth spacecraft occurred in the duration of the interplanetary coronal mass ejection (ICME) driving the shock on 14 December which was related to the 13 December solar event. Solar wind observations from ACE show evidence of the presence of the ICME, which had the enhanced magnetic field and a smooth rotated “magnetic cloud” in the upstream shock and the intervening sheath region, respectively. According to the Wind magnetic cloud list, the axis orientation of this “magnetic cloud” was $\theta = 27^\circ$, $\phi = 85^\circ$. In addition, Liu et al. (2008) estimate that the “cloud” axis direction was $\theta = -57^\circ$, $\phi = 81^\circ$ in GSE coordinates. Thus, both agree that the axis was closely aligned west to east but differ in whether it was inclined north or south, most likely because different intervals were considered in their analysis.

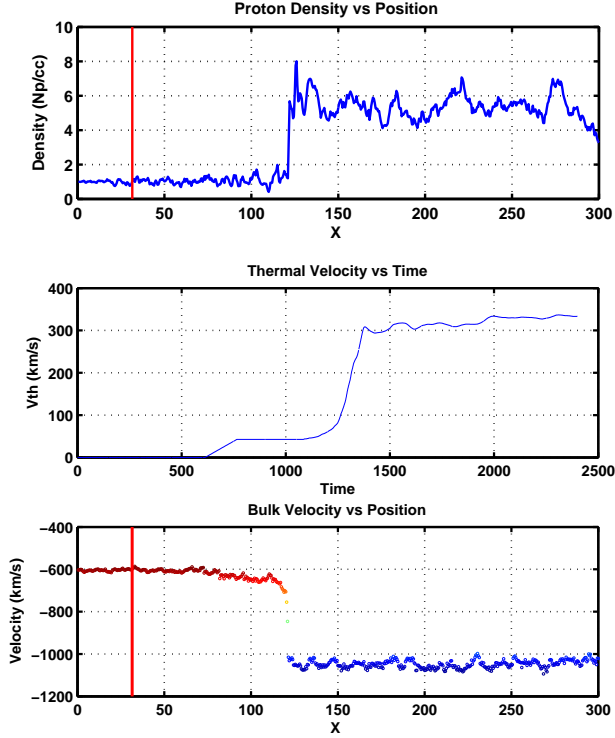


Fig. 2 The upper panel represents the proton density profile vs its position at the end of the simulation. The middle panel denotes the solar wind thermal velocity profile in the local frame vs the time. The lower panel indicates the bulk flow speed profile vs its position at the end of the simulation. The vertical lines in the upper and lower panels both show the final FEB position at the end of simulation.

3 THE METHOD

3.1 Physical model

We consider a plane-parallel shock where the supersonic flow moves from the Sun to the Earth (in the rest frame) along the x -axis direction. The shock was observed by Wind, SOHO, and ACE spacecraft near the Earth in the location of the first Lagrangian point $L1 \sim 1.5$ million km ($\sim 250R_e$, where R_e is the radius of the Earth) upstream of the Earth on 14 December. All trajectories of the spacecraft in the 348th day corresponding to the 14 December 2006 are shown in Figure 3. With the CME-driven shock propagating from the Sun along x -axis to the Earth, its shock front were encountered by Wind, SOHO, and ACE spacecraft located in X_{GSE} between the $250R_e$ and $180R_e$ upstream to the Earth. These three spacecraft moved about $10R_e$ distance in their orbits on the 348th day. The distances of all these three spacecraft from the Sun-Earth line were within $50R_e$ along the Y_{GSE} and Z_{GSE} directions. The 14-Dec-2006 shock event originated from the western hemisphere of the Sun with an interplanetary “magnetic cloud” axis orientation of $\theta = 27^\circ$, $\phi = 85^\circ$. And the actual trajectory of Wind spacecraft at that moment is just tangent to the Sun-Earth line with an angle $\phi = 80^\circ$ as shown in the lower panel of the Figure 3. As far as the position of Wind spacecraft is concerned, the observed CME-driven shock is just a parallel diffusive shock. So the observation of Wind spacecraft provided an example of semi-parallel shock for applying our dynamical Monte Carlo code to understand the particle injection problem of DSA theory.

Table 1 The Parameters of the Simulated Shock

Simulated Parameters		Dimensionless value	Scaled value
Physical	Upstream bulk speed	$u_u=-0.4467$	-600km/s
	Downstream bulk speed	$u_d=-0.7742$	-1042km/s
	Relative inflow velocity	$\Delta u=0.3275$	442km/s
	Inflow sonic Mach number	$M=17.5$...
	Thermal speed	$v_0=0.0342$	46km/s
	Scattering time	$\tau=0.3333$	0.052s
Numerical	Box size	$X_{max}=300$	$10R_e$
	Total time	$T_{max}=2400$	6.3minutes
	Time step size	$dt=1/30$	0.0053s
	Number of zones	$nx=600$...
	Initial particles per cell	$n_0=650$...
	FEB distance	$X_{feb}=90$	$3R_e$

Notes: The physical parameters are taken from the Wind spacecraft, and the numerical parameters are decided by the 14-Dec-2006 CME-driven shock.

The important physical parameters of this simulation include the upstream bulk flow velocity (u_u), the downstream bulk flow velocity (u_d), the relative bulk inflow velocity difference (Δu), the inflow sonic Mach number ($|u_d|/c_s$), which is 17.5 (where $c_s \equiv (\gamma kT/m)^{1/2}$, c_s is the upstream sound speed), the upstream thermal velocity [$v_0 \equiv (kT/m)^{1/2}$], and the constant scattering time (τ), which is 2/5 times of the scattering time ($\tau_0 = 0.13s$) used by Knerr, Jokipii & Ellison (1996) in the Earth-bow shock simulation. Since there are some differences in the shock geometry between the CME-driven shock (i.e. at $L1$ point) and the Earth-bow shock, we chose the scattering time 0.4 times smaller than that in the Earth-bow shock, which is equivalent to a 2.5 times larger FEB distance than that in the Earth-bow shock. The specific physical parameters and numerical parameters are listed in the Table 1 with their dimensionless values and scaled values, respectively.

3.2 Mathematical model

According to the observed 14-Dec-2006 CME-driven shock, the schematic diagram of the simulation box can be designed as one-dimensional parallel shock along the x-axis direction. As shown in Figure 4, the initial particles with a relative bulk flow speed difference (Δu) move from the right to the left. The initial particles have a background Maxwellian thermal distribution with an initial temperature ($T_0 \equiv mv_0^2/k$) in the local frame. To begin and maintain the shock simulation, particles are assumed to flow into the simulation box from the pre-inflow box (PIB) at the right boundary. Then, with the continuous particle flow moving forward one time step, only those particles which move into the main simulation box are actually added to the simulation. This process naturally leads to a flux-weighted inflow population. At the left boundary of the box, a reflective wall acts to produce a CME-driven shock moving from the left to the right. Considering the geometry of the 14 December shock event, we just follow the parallel component of the CME-driven shock observed in Wind spacecraft.

Figure 4 also shows one typical particle and its local (V_L) or box frame (V) velocity in the upstream region and downstream region, respectively. The majority of the incoming particles cross the shock front only once from the upstream region to the downstream region and stay in the downstream region. A small portion of the particles can effectively scatter off the resonant MHD wave self-generated by the energetic particles and return to the upstream region to re-cross the shock front for additional energy gains (Liu, Petrosian & Mason, 2004). Thus an anisotropic energetic particle distribution, but not a strict Maxwellian distribution, is produced in the diffusive regions. It is this elastic interaction between individual particles and the collective background that allows the Fermi acceleration to occur.

The position of the FEB could coincide with a location upstream of the shock where particles are no longer able to scatter effectively and return to the shock. A reasonable FEB farther out in front of the shock moves, accompanying with the shock front, at the same shock evolutionary velocity V_{sh} . This constant FEB distance is acted to inform a precursor region which is showed by the shadow area in the

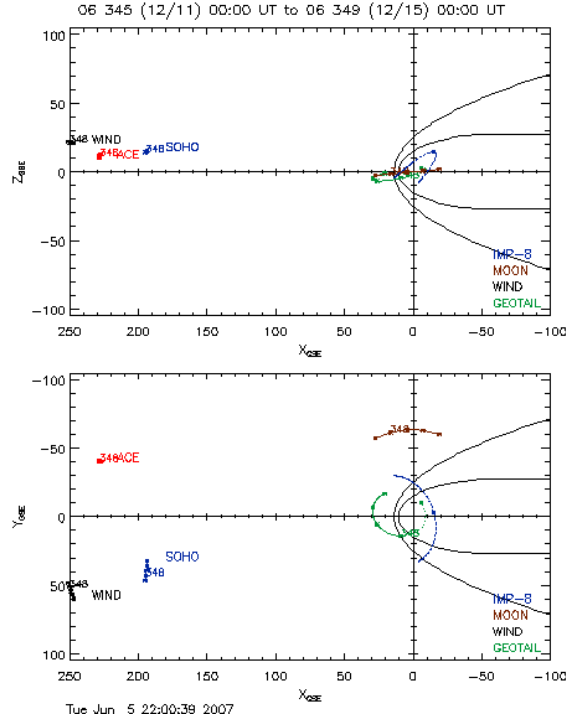


Fig. 3 The diagrams show the realistic orbits of the near-Earth spacecraft. The orbit data are taken from <http://cdaweb.gsfc.nasa.gov/cdaweb>.

middle of the Figure 4. If one particle archives to the highest energy, and exceeds the position of the FEB in front of the shock, it will be taken as the escaped particle and removed from the simulation system. According to the actual motion of Wind spacecraft in the duration, the spacecraft moved about $10R_e$ distance in their orbits on the 348th day. To simulate the shock formation and evolution, the total length of the simulation box is set to be $10R_e$, the length of the FEB is set to be $\sim 3R_e$. The scattering time is set to be $\tau = 0.052s$ on the basis of the Earth-bow shock model (Knerr, Jokipii & Ellison, 1996).

The important numerical parameters include the box size (x_{max}), the time to evolve the whole system (t_{max}), the number of grid zones (n_x), the initial number of particles per zone (n_0), and the size of the time step (dt). Because of the similar character of the plasma flow near the Earth, we take some numerical parameters as in the Earth-bow shock model (Knerr, Jokipii & Ellison, 1996). Specifically, the total box length $x_{max} = 300$ is divided into $n_x = 600$ grids, with each grid length being $\Delta x = 1/2$; the total time $t_{max} = 2400$ is divided into $n_t = 72000$ steps by dt , with each step being $dt = 1/30$. All numerical parameters are listed in Table 1. The physical parameters and the numerical parameters constitute the whole simulation parameter list. As shown in Table 1, each dimensionless value is corresponding to its scaled value. The scale factors for distance, velocity, and time are $x_{scale} = 10R_e/300$, $v_{scale} = 442kms^{-1}/0.3275$, and $t_{scale} = x_{scale}/v_{scale}$, respectively.

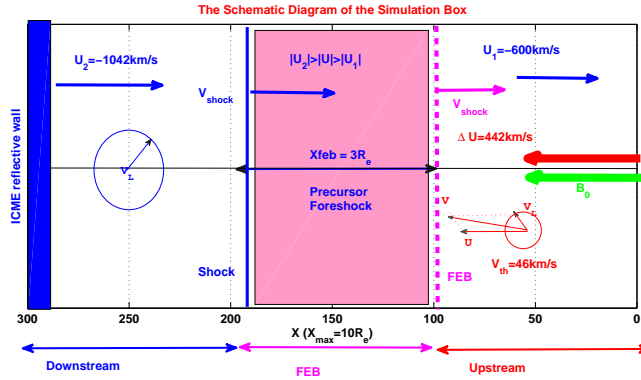


Fig. 4 The schematic diagram of the simulation box. The left reflective wall acts ICME to produce the ICME-driven shock prorogating from the left boundary to the right boundary of the box.

The presented simulations apply the same steps like the Earth-bow shock model (Knerr, Jokipii & Ellison, 1996) including three sub steps: (i) All the particles moving with their velocities in the simulation box along the x axis direction. (ii) Summing particle masses and velocities over each background computational grid. (iii) Invoking the scattering angular distribution law. The particle diffusive processes in the presented simulations are dominated by the Gaussian scattering angular distributions. The scattering rate is $R_s = dt/\tau$, which implies that only this fraction of particles is able to scatter off the scattering center frozen in the background fluid. The candidate does not change its route until it is selected to scatter once again. So the particle's mean free path is proportional to the local thermal velocities in the local frame with

$$\lambda = V_L \cdot \tau. \quad (1)$$

For an individual proton, the grid-based scattering center can be seen as a sum of individual momenta. So these scattering processes can be taken as the elastic collisions. In an increment of time, once all of the candidates complete these elastic collisions, the momentum of the grid-based scattering center is changed. In turn, the momentum of the grid-based scattering center will affect the momenta of the individual particles in their corresponding grid in the next increment time. One complete time step consists of the above three substeps. The total simulation temporally evolves forward by repeating this time step sequence. To calculate the scattering processes accurately and produce an exponential mean free path distribution, the time step should be less than the scattering time (i.e. $dt < \tau$).

The scattering angles consist of two variables: $\delta\theta$ and $\delta\phi$. Once a particle has a collision with the background scattering centers, its pitch angle becomes $\theta' = \theta + \delta\theta$, and the azimuthal angle becomes $\phi' = \phi + \delta\phi$, where $\delta\theta$ is the variation in the pitch angle θ , and $\delta\phi$ is the variation in the azimuthal angle ϕ . The pitch angles θ and θ' are both in the range $0 \leq \theta, \theta' \leq \pi$, and azimuthal angles ϕ and ϕ' are both in the range $0 \leq \phi, \phi' \leq 2\pi$ on the unit sphere. The variation in the pitch angle $\delta\theta$ and azimuthal angle $\delta\phi$ are composed of the scattering angle, and its anisotropic character is described by the Gaussian function $f(\delta\theta, \delta\phi)$. Here, we will just present the results of the CME-driven shock using the Gaussian scattering angular distribution with a standard deviation value of $\sigma = \pi$.

4 RESULTS

4.1 Data analysis

Since the individual particle energy can be examined at any given time in the simulation, so the energy function over time can be obtained. At first, we can calculate the necessary energy functions for further analysis. In this simulation, we obtained the total energy function in the box, the loss energy function escaped from the FEB, and the injected energy function which is the energy summation of the injected energetic particles from the downstream region at the local velocity of $V_L = U_0$ over time. Then, at the end of the simulation, we obtained the final values of the total energy $E_{tot} = 3.5666$, the energy loss $E_{loss} = 0.2010$, and the energy injection $E_{inj} = 0.5464$, respectively. The final energy injection rate R_{inj} , which represents the acceleration efficiency, can be defined by the formula as follows.

$$R_{inj} = E_{inj}/E_{tot} \quad (2)$$

The injection rate is so important for a CME-driven shock, because it is connected with the facts that the shock how distribute itself energy to accelerate cosmic ray (CR) and to “heat” the thermal background plasma. By a series of simulations, we give a plausible injection rate with a value of $R_{inj} = 15.32\%$ for the 14-Dec-2006 shock. Under this condition, we obtain the maximum energy particle with the dimensionless value of $VL_{max} = 20.2609$ and the scaled value of $E_{max} = 3.8684MeV$. In addition, because there exists some energy losses in the simulation system, the shock fine structures do not completely agree with the situ observations. Finally, according to the DSA theory, the energy spectrum index can be calculated based on the simulated compression ratio (i.e., $\Gamma = (r + 2)/[2(r - 1)]$). We calculated the total energy spectral index with a value of $\Gamma_{tot} = 0.8406$ and the vicious subshock energy spectral index with a value of $\Gamma_{sub} = 1.1074$, respectively.

Figure 5 shows the simulated energy spectra. The first plot shows the energy spectrum with the “double-peak” structures averaged over the entire simulation box at the end of the simulation. The second plot shows an energy spectrum with a “power-law” tail averaged only over the downstream region at the end of the simulation. In this plot, the thick solid curve with a narrow peak represents the initial Maxwellian thermal energy spectrum in the shock frame. As viewed from the first plot, the double peaks imply that there exist two thermal particle distributions in the entire simulation box: the left peak represents the “heated” downstream flow distribution and the right peak represents the Maxwellian distribution in the unshocked upstream flow. Turn to look at the second plot, we find the final extend energy spectrum at the left of the panel shows several decade times wider than that in the initial energy spectrum at the right of the panel. This means that there exist a large temperature difference between the shocked downstream region and the unshocked upstream region.

As shown in Figure 6, the spectra of protons in the two largest December 2006 SEP events by ACE, STEREO, and SAMPEX instruments are reported. The particle intensities started increasing at the beginning of the December 5 and the other at the onset of the December 13 event. These two events both have spectra that roll over in a similar fashion beyond $\sim 50MeV$, as in the 20-Jan-2005 SEP event (Mewaldt et al., 2008; Wang, Zhao, & Zhou, 2009; Bartoli et al., 2012; Wang et al., 2010). The fitting energy spectral shape of the 12-14 December 2006 events are showed in the lower panel and the spectral index is marked as a value of $E^{-1.07}$ in the lower energy range. The predicted subshock energy spectral index ($\Gamma_{sub} = 1.1074$) from our simulation is consistent with the observed energy spectral index in the lower energy range. Owing to computer constraints on the size of the simulation grid, this simulated energy spectrum is just in the range from keV to MeV. We speculate that the second “roll over” on the higher energy spectrum could be obtained if a larger simulation box size is used. This will be investigated in a future simulation. There are two conditions suggesting that the “roll-over” would be reproduced at high energy: (1) The FEB distance decides the maximum diffusive length (i.e. $FEB \equiv \lambda_{max} = \tau \cdot p_{max}$). If we enlarge the FEB distance and the total simulation box, we can obtain the larger P_{max} in the new simulation system. (2) In the Figure 6, we can see the first power law $E^{-1.07}$ as the input function of the second power law $E^{-2.45}$ at the high energy range. Simultaneously, in the Figure 5, we can see the heated Maxwellian thermal distribution, which would be represented by

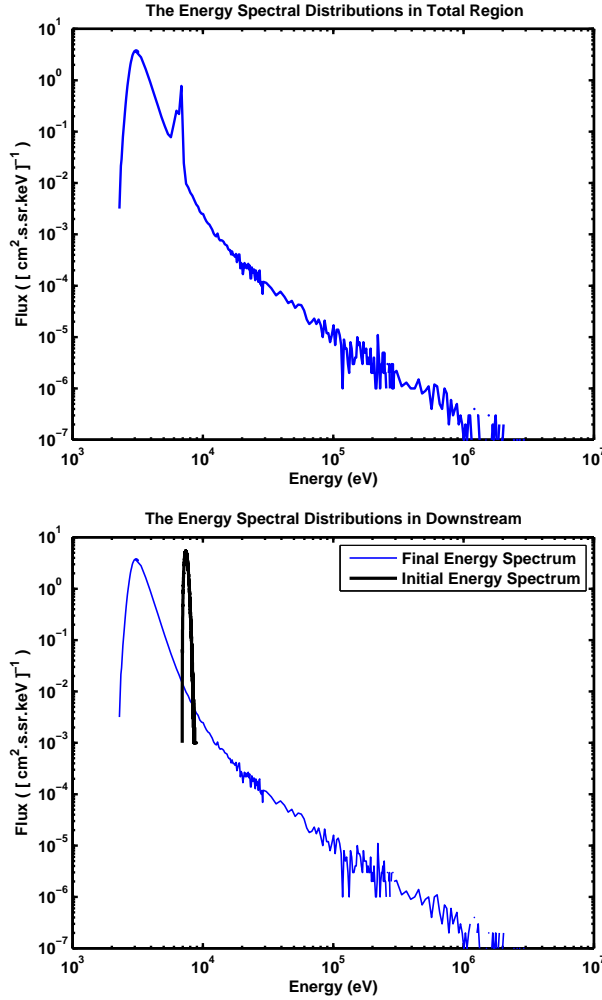


Fig. 5 The extend energy spectra in two plots are calculated over the entire simulation region and the only downstream region at the end of the simulation, respectively. The solid extended curve with a “power-law” tail in each plot represents the final shocked energy spectrum. The thick curve with a narrow peak denotes the initial Maxwellian energy spectrum.

a similar power law $E^{-0.5}$ averaged over the respective energy range, as the input function of the first power law $E^{-1.1074}$.

4.2 Shock structures

At the end of the simulation, the simulated shock with the specific parameter values are given as follows: the shock position $X_{sh} = 121.5$, the FEB position $X_f = 31.5$, the shock evolutionary velocity $V_{sh} = -0.0744$, the subshock velocity $V_{sub} = 0.2103$, total compression ratio $r_{tot} = 5.4034$, subshock’s compression ratio $r_{sub} = 3.4697$, total energy spectral index $\Gamma_{tot} = 0.8406$, subshock’s energy spectral index $\Gamma_{sub} = 1.1074$, particle injection rate $R_{inj} = 15.32\%$, energy loss $E_{loss} = 0.2010$,

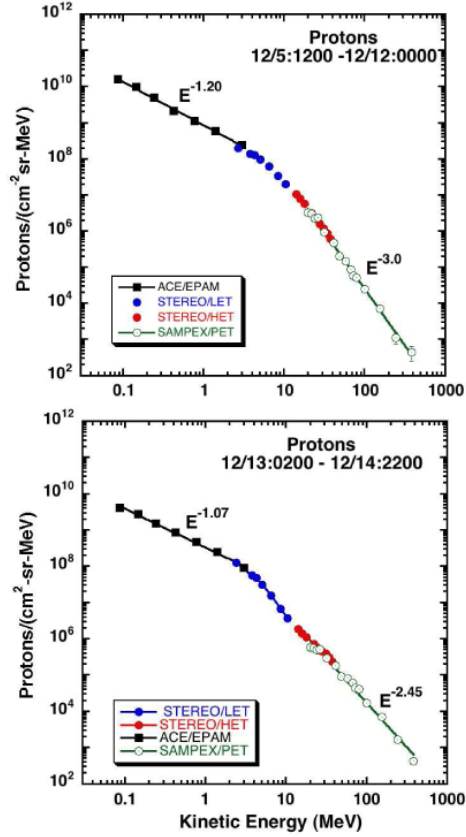


Fig. 6 Fluency spectra of the protons measured in the two largest December 2006 SEP events by multiple spacecraft. The energy range is from 5 to 100 MeV adapted from Mewaldt et al. (2008).

the maximum energy particle's local velocity $VL_{max} = 20.2609$, and the maximum energy particle $E_{max} = 3.8684 MeV$.

First, we present the entire shock evolution with the temperature profile of the time sequences as shown in Figure 7. The supersonic continuous inflow with an initial Maxwellian thermal velocity v_0 in each grid evolves from the begin to the end of the simulation. Their kinetic energies are translated into the random thermal energetic particles by the “heating” processes in the downstream region resulting in a distinct enhancement temperature profiles in the shock front with the time. The profile of the thermal temperature shows the upstream averaged temperature of $T_0 = 2.5 \times 10^5 K$ and the downstream averaged temperature of $T_d = 9.0 \times 10^6 K$. This means that the CME-driven shock can “heat” the background plasma efficiently and provide the first-order Fermi acceleration mechanism by crossing

the shock front for accelerating the particles, which are injected from the “heated” downstream region into the precursor region.

Figure 2 shows a group of profiles of the physical parameters in the simulation. From top to bottom, the upper panel shows the proton density profile vs its position. The proton density is presented by the scaled value. The enhanced density flux apparently appears in the position of the shock front. The intensity of the density in the downstream is about five times larger than those in the unshocked upstream bulk flow. By comparing the proton density profiles between the the Figure 2 and the Figure 1, the simulated bulk flow has a lightly higher proton density intensity in the downstream bulk flow than that in the observed downstream bulk flow. The middle panel in the Figure 2 denotes that the thermal velocity profile evolves with the time. The profile at time of $T \sim 600$ (it is zero before the simulation time $T < 600$, take account of the injection from the PIB) has an initial Maxwellian thermal velocity of $v_0 = 46 \text{ km/s}$ until it is shocked. After the profile is shocked as shown in middle panel of the Figure 2, it reaches an average thermal velocity with a value around $\langle v_d \rangle = 300 \text{ km/s}$ till the end of the simulation. Also the thermal velocity profile shows a slightly larger enhancement than that from the observation by Wind spacecraft. Although the simulated proton density and the solar wind thermal velocity are slightly larger than those from in-situ observations, we suggest that this is caused by the insufficiency of particles in the simulation. We have demonstrated that it is the case using a series of simulations with different initial number of particles per cell. The lower panel indicates the profiles of the bulk flow speed vs its position at the end of the simulation. The profile shows an upstream bulk flow speed $U_u = -600 \text{ km/s}$ and the downstream bulk flow speed $U_d = -1042 \text{ km/s}$ which are followed by the observations. The complex shock front fine structure will be showed in Figure 8 at the end of the simulation. The final evolutionary positions of the FEB and the shock front are $X_f = 31.5$ and $X_{sh} = 121.5$ in the x-axis, respectively. The distance between these two locations is just the size of the precursor region where the particle acceleration processes occur. It is just this region slowed the incoming upstream bulk flow speed U_u down to the downstream bulk flow speed U_d . The bulk flow speed in precursor region is between the two bulk flow speeds (i.e. $U_u > U_p > U_d$). From our simulation, we can see that the particle acceleration process and the “back pressure” due to the energetic particles occurred mostly in precursor region which results in a non-linear shock structure that is characterized by a bulk flow speed gradient. According to the evolutionary shock front position X_{sh} with the time, we can calculate the shock evolutionary velocity V_{sh} as follows.

$$V_{sh} = \frac{|X_{max} - X_{sh}|}{T_{max}}, \quad (3)$$

where, the X_{max} is the total length of the simulation box, and the T_{max} is the total simulation time. Then, we are able to calculate the total shock compression ratio in the shock frame as follows.

$$r_{tot} = \frac{\Delta U + |V_{sh}|}{|V_{sh}|}, \quad (4)$$

where ΔU is the relative bulk flow speed between the upstream and downstream, V_{sh} is the shock velocity.

Figure 8 shows the shock fine structure with the bulk flow speed near the shock front at the end of the simulation. $V_{sub} = 0.2103$ shows the bulk flow speed of the subshock, $V_d \simeq 0$ shows the bulk flow speed of the downstream region, $V_{sh} = -0.0744$ represents the value of the opposite shock evolutionary velocity, and $U_0 = 0.3275$ represents the incoming bulk flow speed with a related bulk flow speed difference of ΔU . All zones of the precursor, subshock and downstream are divided by a vertical dashed line and a solid line in the plot. These three zones constitute the total shock fine structure in the simulated shock region. The smooth precursor has a long scale in the range from the subshock’s position X_{sub} to the FEB position X_f , which is invisible, beyond the left boundary of the plot. This zone is called the diffusive zone where the bulk flow speed will be slowed by the “back pressure” of the accelerated particles. The subshock region with a narrow scale of a three-grid-length has a deep drop of the bulk flow speed, in which the bulk flow speed vary from the subshock velocity V_{sub} to the downstream velocity V_d . The scale of the three-grid-length is almost identical to the averaged thermal

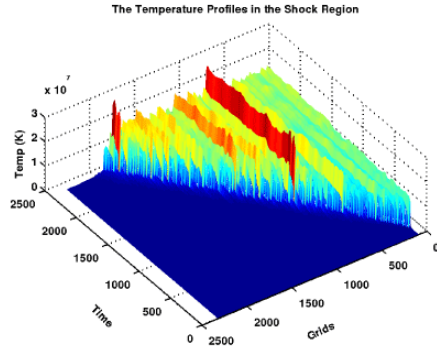


Fig. 7 The mesh plot represents the evolutionary bulk flow temperature profiles in their positions with the time. The lower temperature represents the upstream bulk flow. The higher temperature represents the downstream bulk flow. The apparently distinguished boundary traces the shock front positions with time.

mean free path over the downstream region. The subshock velocity V_{sub} is decided by the horizontal dot-dashed line with a value of $V_{sub} = 0.2103$. The downstream velocity V_d is marked with a horizontal dashed line at the end of the simulation, which should be with an averaged value of $\langle V_d \rangle = 0$ over the entire simulation time in the box frame. The negative shock evolutionary velocity marked with a horizontal solid line shows a value of $V_{sh} = -0.0744$. We can calculate the subshock's compression ratio according to Rankie-Hongniout relationships in the shock frame as follows.

$$r_{sub} = \frac{V_{sub} + V_{sh}}{\langle V_d \rangle + V_{sh}}, \quad (5)$$

where, we take the averaged value of the downstream velocity $\langle V_d \rangle$ equal to zero.

5 SUMMARY AND CONCLUSIONS

In summary, we performed a dynamical Monte Carlo simulations on the 14-Dec-2006 CME-driven shock using an anisotropic scattering law. The specific temperature profile, shock fine structures, particle injection function, as functions of time, are presented. We examined the correlation between the energy injection and the shock energy translation processes of the interplanetary CME-driven shock. Simultaneously, we find the simulated CME-driven shock energy spectrum provides a good fit to the observations from the multiple spacecraft.

In conclusion, the dynamical Monte Carlo simulation of the 14-Dec-2006 CME-driven shock demonstrates that the energy spectrum is affected by the specific non-linear factor of the DSA. This paper focus on the energy injection, which is one of important nonlinear effects of the DSA. By calculating the energy injection rate of the CME-driven shock, we can understand how the CME-driven shock distributes its shock energy to accelerate the energetic particles by first-order Fermi acceleration mechanism as well as how it heats the solar wind background bulk flow at a certain efficiency. We give an energy injection rate of $R_{inj} = 15.32\%$ in the 14-Dec-2006 CME-driven shock. We guess that this predicted injection rate could satisfy the required energies of the observed SEP events, which should be released from the CME-driven shock.

Acknowledgements The work was supported by the Chinese Academy Sciences NSFC grant 10921303, and the National Basic Research Program of the MOST Grant (No. 2011CB 811401).

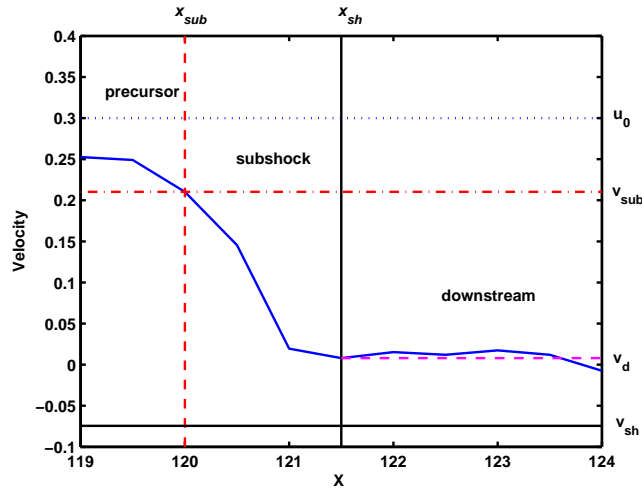


Fig. 8 The bulk flow speed fine structure of the simulated shock at the end of the simulation. The vertical dash line and vertical solid line split the entire region into three sections: precursor, subshock and downstream region.

References

- Axford, W.I., Leer, E., & Skadron, G., 1977, in Proc. 15th Int. Cosmic Ray Conf. (Plovdiv), 132
- Bartoli B., et al., 2012, ApJ, 745, L22
- Baring, M. G., Ogilvie, K. W., Ellison, D. & Forsyth, R. 1997 ApJ, 476, 889.
- Bell, A. R., 1978, MNRAS, 182, 147.
- Bednarz, J. & Ostrowski, M., 1999, MNRAS310, L13.
- Berezhko, E.G., & Völk, H. J., 2000, A&A, 357, 283
- Blandford, R. D., & Ostriker, J. P., 1978, ApJ, 221, L29.
- Bykov, A. M. & Treumann, R. A. , 2011, A&A Rev., 19, 1, 42.
- Bykov, A. M., Uvarov, Yu. A., Bloemen, J. B. G. M., den Herder, J. W., Kaastra, J. S., 2009, MNRAS, 399, 1119-1125,
- Caprioli, D., Amato, E., Blasi, P., 2010, *Astropart. Phys.*, 33, 307
- Cane H. V., Reames D. V., von Rosenvinge T. T., 1991, ApJ, 373, 675
- Drury L. O., Völk J. H., 1981, ApJ, 248, 344
- Drury L. O., Axford W. I., Summers D., 1982, MNRAS, 198, 833
- Ellison, D. C. & Eichler, D., 1984, ApJ, 286, 691
- Ellison, D. C., Möbius, E. & Paschmann, G. 1990, ApJ, 352, 376.
- Hu H., 2009, epreprint (arXiv/0911.3034)
- Kang H. & Jones T. W., 2007, *Astropart. Phys.*, 28, 232
- Knerr, J. M., Jokipii, J. R. & Ellison, D. C. 1996, ApJ, 458, 641
- Krymsky, G. F., 1977, Akad. Nauk SSSR Dokl., 243, 1306
- Le G., Cai Z., Wang H., Zhu Y., 2011, Ap&SS, 745
- Li C., Dai Y., Vial J.-C., Owen C. J., Matthews S. A., Tang Y. H., Fang C., Fazakerley A. N., 2009, A&A, 503, 1013
- Li G., Zank G. P., 2005, GeoRL, 32, 2101
- Liu, Y., Luhmann, J. G., Müller-Mellin, R., et al., 2008, ApJ, 689, 563.
- Liu S., Petrosian V., Mason G. M., 2004, ApJ, 613, L81
- Lu Q. M., Xia L. D., Wang S., 2006, JGRA, 111, 9101

- Malkov, M. A., Drury L.O'C., 2001, *Rep. Prog. Phys.*, 64, 429
- Malkov, M. A., Diamond, P. H. & Völk, H. J., 2000, *ApJ*, 533, L171
- Mewaldt, R. A., Cohen, C. M. S., Cummings, A. C., et al. 2008, 30th International Cosmic Ray Conference, Int. Union of Pure and Appl. Phys., Mrida, Mexico. Vol.1 (SH) 107-110.
- Miller J. A., 1997, *ApJ*, 491, 939
- Mulligan, T., Blake, J. B. & Mewaldt, R. A., 2008, 30th International Cosmic Ray Conference, Int. Union of Pure and Appl. Phys., Mrida, Mexico. Vol.1 (SH) 179.
- Pick M., Vilmer N., 2008, *A&ARv*, 16, 1
- Qin G., Shalchi A., 2009, *ApJ*, 707, 61
- Reames D. V., Meyer J. P., von Roseninge T. T., 1994, *ApJS*, 90, 649
- Vladimirov, A. E., Ellison, D. C. & Bykov, A., 2006, *ApJ*, 652, 1246
- von Roseninge T. T., Richardson, I. G., Reames, D. V., et al., 2009, *Solar Phys.*, 256, 443-462. doi:10.1007/s11207-009-9353-6
- Verkhoglyadova, O. P., Li, G., Zank, G. P., et al. 2010, *J. Geophys. Res.*, 115, A12103, doi: 10.1029/2010JA015615
- Wang B., Yuan Q., Fan C., Zhang J., Hu H., Bi X., 2010, *ScChG*, 53, 842
- Wang J., Shi Z., Wang H., Lue Y., 1996, *ApJ*, 456, 861
- Wang J., Zhao M., Zhou G., 2009, *ApJ*, 690, 862
- Wang S. J., Yan Y. H., Liu Y. Y., Fu Q. J., Tan B. L., Zhang Y., 2008, *SoPh*, 253, 133
- Wang, X., & Yan, Y., 2011, *A&A*, 530, A92,
- Wang, X., & Yan, Y., 2012, preprint (astro-ph/1111.0162)
- Yan Y., Pick M., Wang M., Krucker S., Vourlidas A., 2006, *SoPh*, 239, 277
- Zhang J., Dere K. P., Howard R. A., Kundu M. R., White S. M., 2001, *ApJ*, 559, 452
- Zhang J.-L., Bi X.-J., Hu H.-B., 2006, *A&A*, 449, 641
- Zhang J., Solanki S. K., Woch J., Wang J., 2007, *A&A*, 471, 1035
- Zirakashvili, V. N., 2007, *A&A*, 466, 1-9,